Hindawi
Shock and Vibration
Volume 2017, Article ID 1634292, 16 pages
https://doi.org/10.1155/2017/1634292

Research Article

Study on Galloping Oscillation of Iced Catenary System under Cross Winds

Guo Chen, Yiren Yang, Yang Yang, and Peng Li

School of Mechanics and Engineering, Southwest Jiaotong University, Chengdu, Sichuan 610031, China

Correspondence should be addressed to Guo Chen; apple88125@hotmail.com

Received 2 June 2017; Revised 29 August 2017; Accepted 6 September 2017; Published 22 October 2017

Academic Editor: Tai Thai

Copyright © 2017 Guo Chen et al. This is an open access article distributed under the Creative Commons Attribution License, which permits unrestricted use, distribution, and reproduction in any medium, provided the original work is properly cited.

This paper mainly aims at revealing the nature of the galloping oscillation of iced catenary system under cross winds. The aerodynamic force on the iced catenary system is assumed to be quasi-steady, and then the quasi-steady aerodynamic lift and drag coefficients are completed in FLUENT. By fitting the discrete simulation data, the expression of the vertical aerodynamic force is further obtained. According to the Den Hartog vertical galloping mechanism, the stability of iced catenary is discussed and the initial icing angle corresponding to the critical stability is obtained. On this basis, the dynamic model of the simple iced catenary system under cross winds is established. The partial differential vibration equation of the system is converted into the ordinary differential equation by the Galerkin method and then numerically solved. The condition of the unstable catenary motion in simulation is in agreement with that from theoretical stability analysis. In addition, the effects of structural damping, initial icing angle, and wind velocity on the system responses are investigated.

1. Introduction

High speed train is driven by electric locomotives which gain electrical power from pantograph-catenary system. Therefore, proper functioning of catenary is one of the key factors that guarantee the operating safety of high speed railway. With the wide application of electrified railway, the working environment is complicated and various. Especially for areas of low temperature and high humidity and altitude, it is extremely likely for catenary to be covered with ice. Covering ice can not only severely affect the current collecting quality, but also cause a large amplitude oscillation of catenary under cross winds, which may lead to withdrawn train and equipment damage [1]. Generally speaking, this kind of vibration is known as galloping, which is also called dancing [2]. Due to the widespread existence of galloping phenomenon, it is of great significance for engineers to master the dynamic characteristics of catenary system with galloping oscillation.

Investigations on iced conductor galloping have been of interest to researchers for decades. Den Hartog [3] proposed the vertical galloping criterion. He found that after icing changed the cross section of conductor, under certain wind velocity and angle of attack, when the negative slope of lift force curve was larger than the amplitude of drag force curve, the occurrence of instability phenomenon could cause the conductor galloping in the vertical direction. Nigol and Buchan further verified the galloping theory mentioned in [4] by the wind tunnel experiment. Additionally, Nigol and Buchan [5] found that when the vertical galloping condition was not satisfied, the galloping would also be caused by the self-excited torsional vibration of iced conductor. Aiming at the galloping mechanism, Yu et al. [6, 7] proposed the novel suggestion that the galloping was caused by the eccentricity inertia of cross section of iced conductor.

Taking a linearized lumped parameter system with two degrees of freedom as the research object, Luongo and Piccardo [8] analyzed the bifurcation characteristic of the system with galloping by the perturbation approach. Jones [9] studied the linearized coupled vertical-horizontal galloping behavior analytically and drew the conclusion that the coupled galloping criterion might be either more or less stringent than Den Hartog's criterion. In reference [10], a comprehensive analysis was presented for the galloping of an oscillator that might vibrate both transversely and torsionally.

Furthermore, a three-degree-of-freedom model for galloping was developed and analyzed analytically in [11, 12].

In the previous work, the galloping model was usually considered as a lumped model. Actually, the continuous characteristics of multispan conductor are extremely important and should not be ignored. In view of this, Desai et al. [13] described the galloping behavior of the multispan iced transmission line by the finite element method, in which the three-node isoparametric cable element included torsional and three translational degrees of freedom at each node. Since then, the finite element method has been widely used in the galloping research. Based on the work mentioned in [13], Desai et al. [14] developed an efficient perturbation method to calculate the galloping vibration of the multispan overhead transmission line. Zhang el al. [15] established a computationally efficient hybrid model, in which the mode shapes were determined by the finite element method and the initial condition, and analytically investigated the steady vibration amplitudes of the system. Keutgen and Lilien [16] conducted a wind tunnel test to obtain a full set of data of recent galloping results, which were validated by the corresponding numerical simulation. By using the spatial curved beam theory, Yan et al. [17] considered the nonlinearity and bending stiffness of iced conductor, and then presented the finite element model, including three translational degrees of freedom and three rotational degrees of freedom.

In the aspect of catenary galloping, Stickland et al. [18] analyzed the aerodynamic characteristics of a series of contact wires by experiment and determined the occurrence conditions of vertical galloping for different contact wires based on the Den Hartog criterion. Meanwhile, the effects of mechanical damping on the occurrence conditions of galloping were introduced in [18]. Xie et al. [19] conducted a series of wind tunnel tests on the 2 : 1 scaled model of iced contact wires and obtained the relation between aerodynamic force coefficients and angles of attack in the different turbulent flow fields. Besides, the galloping stability of iced contact wire was discussed by them. Song et al. [20] studied the wind-induced vibration of the contact wire with different thickness of ice coating and concluded that the thicker the ice coating was, the more serious the wind deviation of contact wire could get. Meanwhile, literature [20] stated that the influence of average wind load was so little while the fluctuating wind load had a significant effect on the current collecting quality. As for the wind-induced vibration of high speed catenary, the dynamic behaviors of the pantograph-catenary under stochastic wind field were analyzed in reference [21].

Up to now, galloping as well as wind deviation of a single contact wire and fluctuating wind response of iced contact wire has been studied in detail. However, the attention that has been paid to the galloping behavior of the whole iced catenary is not sufficient. In this paper, the galloping behavior of iced catenary system under average cross winds is studied. To this end, the quasi-steady aerodynamic force coefficients of iced contact wire are simulated by FLUENT. The condition of critical instability obtained from the Den Hartog criterion is verified by simulating the system response. On this basis, the phenomenon of low frequency and large amplitude vibration of catenary system under cross winds is explained.

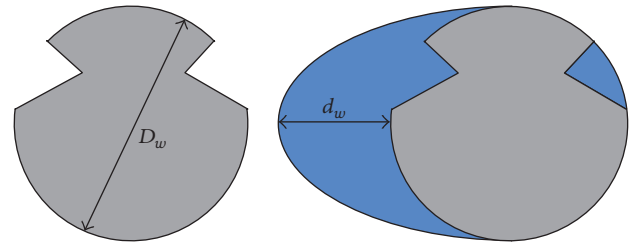

(a) Without ice coating (b) With ice coating

Figure 1: Two kinds of cross section of contact wire.

Moreover, the effects of initial icing angle, damping, and wind velocity on the galloping characteristics of catenary system are discussed in detail.

2. Quasi-Steady Aerodynamic Force of Iced Contact Wire

As one of typical slender structures in the actual engineering, catenary system is mainly composed of messenger wire, contact wire, and droppers. In certain circumstance, slender wires may be covered with ice and then their cross sections would become asymmetric. As a result, average cross winds can cause the galloping vibration of the iced wires under some certain conditions. Previous engineering cases have illustrated that the mean lift and drag coefficients obtained under static conditions can accurately describe the galloping phenomenon [22]. Here the mean lift and drag coefficients are the functions of the angle of attack. Therefore, in this paper, quasi-steady aerodynamic force is used to describe the action of cross winds on the catenary system.

The cross sections of contact wire without and with ice coating are shown in Figure 1. For the case of no ice coating, the contact wire has a circular cross section with two side grooves, which are used to install clamps. The diameter of cross section of contact wire is $D_w = 14.4$ mm [25].

The ice coating shown in Figure 1(b) is assumed ideal crescent, and then an ice shape coefficient [26] is introduced to describe the relation between ice thickness and diameter of cross section; namely,

$$\lambda_w = \frac{D_w}{D_w + d_w}, \tag{1}$$

where d_w is the thickness of ice coating and the value range of λ_w is usually $[1.2, 1.8]$. In this paper, the coefficient is $\lambda_w = 1.6$, indicating that the thickness of ice coating is $d_w = 8.64$ mm.

To simulate the aerodynamic force on the catenary system, the flow is considered two-dimensional and uniform. The cross section of contact wire is fixed in the flow field. According to [27], the drag force and the lift force, respectively, satisfy

$$\begin{aligned} F_{l,w}(\alpha_w) &= \frac{1}{2}\rho_{\text{air}} U^2 D_{r,w} C_{l,w}(\alpha_w), \\ F_{d,w}(\alpha_w) &= \frac{1}{2}\rho_{\text{air}} U^2 D_{r,w} C_{d,w}(\alpha_w), \end{aligned} \tag{2}$$

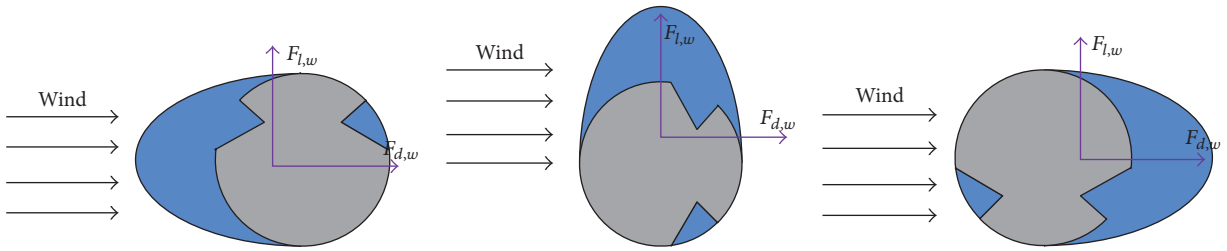

Figure 2: Definition of angle of attack.

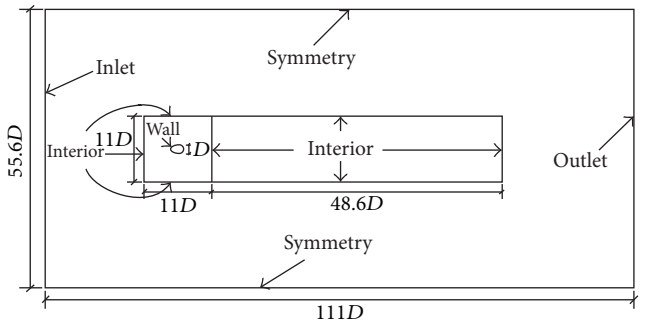

(a) The boundary condition

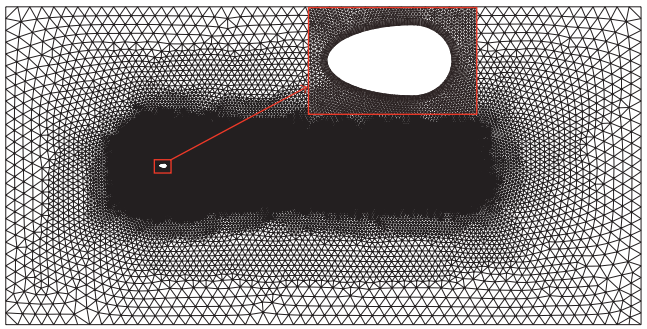

(b) The mesh of flow field

Figure 3: Schematic diagram of computational field in FLUENT.

where $F_{d,w}$ and $F_{l,w}$ denote the drag force and lift force, $C_{d,w}$ and $C_{l,w}$ denote the drag coefficient and lift coefficient, α_w denotes the angle of attack, ρ_{air} denotes the air density, U denotes the wind velocity, and $D_{r,w}$ denotes the maximum height of windward side of cross section and it is approximately equal to the diameter of cross section.

It is shown in Figure 2 that the range of angle of attack is in $[0^\circ, 180^\circ]$. To simulate the aerodynamic characteristics of iced contact wire under cross winds more accurately, the increment of angle of attack is set to 10° in the CFD simulations, meaning that there are 19 simulation cases.

CFD simulations in this paper are carried out by FLUENT in which the Finite Volume Method is applied to spatially discretize the governing equations. The boundary conditions and mesh of the computational field for $\alpha_w = 0^\circ$ are shown in Figure 3, where the computational field is divided into three parts. The left boundary is velocity inlet and the right boundary is flow outlet. The top boundary and bottom boundary are considered as symmetry. Besides, the wall of cross section of iced contact wire is set as no-slip wall. Due to the drastic changes of the flow field near the cross section wall and in the wake region, the grids should be further densified in these two regions. The unstructured grids are applied all over the computational domain and the corresponding total grid number is 140,000. In order to ensure the computational precision, the boundary layer mesh is needed in the near-wall region.

Since the quasi-steady aerodynamic forces can describe the galloping process accurately, the Reynolds-Averaged Navier-Stokes (RANS) equations, in which the transient quantity in the Navier-Stocks equations is decomposed into mean and fluctuating quantities, are considered here. SST k-ω model is recommended as the viscous model in this work. It is a two-equation eddy-viscosity turbulence model which does not need the wall-function and plays a good performance on the adverse pressure gradient, such as flow around a circular cylinder while the Reynolds number is large. SIMPLE-type pressure-velocity coupling scheme is used and second-order upwind scheme is applied to discretize the momentum, turbulent kinetic energy, and the specific dissipation rate. During the simulation process, drag and lift coefficients of the cross section wall are monitored. Wind velocity is set to 15 m/s, time step is specified as 0.1 ms, and the total simulation time is 1 s. The time series data of the first 0.5 seconds are deliberately excluded from the total time series data to ensure that the data used correspond to the steady state.

The Reynolds number of the iced contact wire is $\text{Re} = 21110$ which belongs to the subcritical region. In the subcritical region, the vortex street of the wake region becomes turbulent gradually while the separation of boundary layer appears because of the strong inverse pressure gradient near the iced section wall. Figure 4 is the velocity contour maps of the flow field near the wire section wall under different angles of attack. From the figures the turbulent flow and the separation of boundary layer can be seen clearly.

In accordance with the symmetry of cross section of iced contact wire, the drag and lift coefficients follow the following relationships.

$$C_{d,w}(\alpha_w) = C_{d,w}(-\alpha_w),$$
$$C_{l,w}(\alpha_w) = -C_{l,w}(-\alpha_w). \quad (3)$$

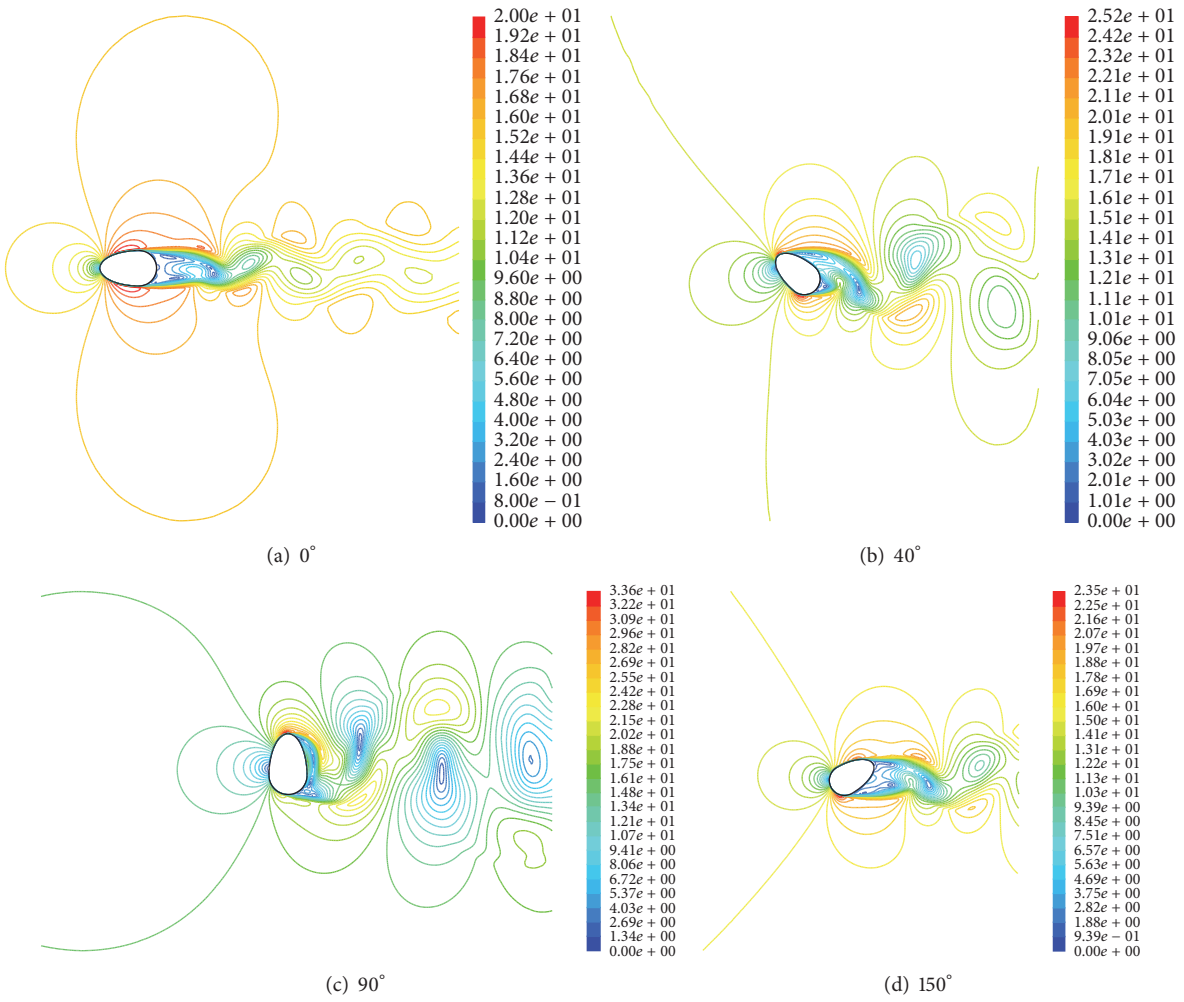

Figure 4: Velocity contour maps under different angles of attack.

According to the time-averaged value of the calculated data, the relations between drag coefficient, lift coefficient, and angle of attack are depicted in Figure 5.

It is clear that when the angle of attack is near ±0° and ±180°, the drag coefficient reaches the minimum because that is when the windward side is the smallest, while the drag coefficient reaches the maximum when the angle of attack is near ±90° because that is when the windward side is the largest. As for the lift coefficient, the peaks appear when the angle of attack is near 40°, 170°, and −130°, and the troughs appear when the angle of attack is near −40°, −170°, and 130°. The changing rules of drag and lift coefficients are in agreement with the wind tunnel test data in [16].

To further verify the results of CFD, aerodynamic coefficients of bluff body section such as a D-shape section and a square section of iced conductor are performed by FLUENT. The model parameters of D-shape section and square section are referred to in [23] and [24], respectively. Figures 6 and 7 show the comparison between the results obtained by CFD in this work and the wind tunnel test results obtained in [23, 24]. It can be seen from the pictures that the coefficients of drag and curves fitted from CFD and wind tunnel tests have uniform tendency.

3. Vertical Aerodynamic Force Model

The galloping model of iced contact wire is shown in Figure 8, in which U is the wind velocity, $\dot{y}_w$ is the vertical vibration velocity, and U_r is the relative velocity between U and $\dot{y}_w$.

The angle between aerodynamic drag force and central line of cross section of iced contact wire is described by α_w, which is usually called angle of attack in the aerodynamics. Additionally, $\alpha_{0,w}$ denotes the initial icing angle, and $\alpha_{r,w}$ denotes the relative angle of attack. Therefore, the specific geometric relationship between them can be expressed as

$$\alpha_w = \alpha_{0,w} - \alpha_{r,w}, \tag{4}$$

$$\alpha_{r,w} = \arctan \frac{\dot{y}_w}{U_r} \approx \frac{\dot{y}_w}{U}. \tag{5}$$

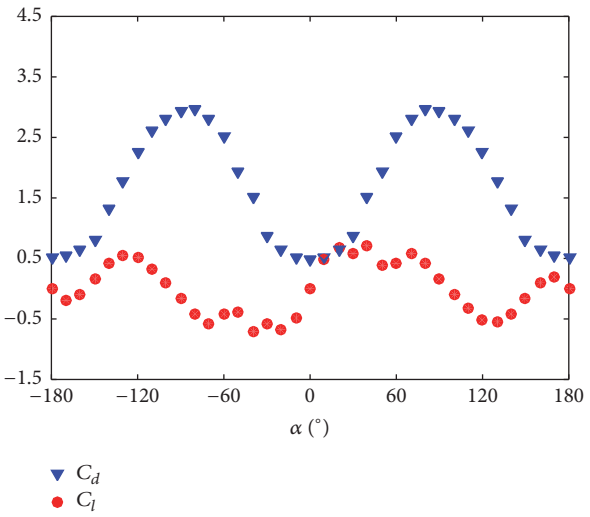

FIGURE 5: Relations between C_d, C_l, and α.

Since the vertical galloping velocity is far less than the wind velocity, U_r is approximately equal to U. The component of drag and lift forces on the axis y_w can be expressed as

$$F_{y,w} = -F_{d,w} \sin \alpha_{r,w} + F_{l,w} \cos \alpha_{r,w}. \tag{6}$$

By substituting (2) into (6), (6) can be further derived as

$$F_{y,w} = \frac{1}{2} \rho_{\text{air}} U^2 D_w C_{y,w}, \tag{7}$$

where $C_{y,w}$ obeys

$$C_{y,w} = -C_{d,w}(\alpha_w) \sin \alpha_{r,w} + C_{l,w}(\alpha_w) \cos \alpha_{r,w}. \tag{8}$$

Aiming at the range of angle of attack $[-50^\circ, 50^\circ]$, the drag and lift coefficients are gradually extracted and then used in the cube polynomial fitting; namely,

$$\begin{aligned} C_{d,w}(\alpha_w) &= d_3 {\alpha_w}^3 + d_2 {\alpha_w}^2 + d_1 \alpha_w + d_0, \\ C_{l,w}(\alpha_w) &= l_3 {\alpha_w}^3 + l_2 {\alpha_w}^2 + l_1 \alpha_w + l_0, \end{aligned} \tag{9}$$

where the polynomial coefficients d_0, d_1, d_2, and d_3 are shown in Table 1. Correspondingly, the fitting curves of drag coefficient and lift coefficient are shown in Figure 9.

By substituting (4) into (9), (8) is further expressed as

$$\begin{aligned} C_{y,w}(\alpha_{r,w}) = &-\left[d_3 (\alpha_{0,w} - \alpha_{r,w})^3 + d_2 (\alpha_{0,w} - \alpha_{r,w})^2 \right. \\ &\left. + d_1 (\alpha_{0,w} - \alpha_{r,w}) + d_0\right] \sin \alpha_{r,w} + \left[l_3 (\alpha_{0,w} - \alpha_{r,w})^3 \right. \\ &\left. + l_2 (\alpha_{0,w} - \alpha_{r,w})^2 + l_1 (\alpha_{0,w} - \alpha_{r,w}) + l_0\right] \cos \alpha_{r,w}. \end{aligned} \tag{10}$$

Assuming the relative angle of attack $\alpha_{r,w}$ is rather small at the very beginning of galloping, (10) can be expanded at $\alpha_{r,w} = 0$ by the Taylor expansion method, so that

$$\begin{aligned} C_{y,w}(\alpha_{r,w}) = &\left. C_{y,w}\right|_{\alpha_{r,w}=0} + \left.\frac{\partial C_{y,w}}{\partial \alpha_{r,w}}\right|_{\alpha_{r,w}=0} \alpha_{r,w} \\ &+ \frac{1}{2!} \left.\frac{\partial^2 C_{y,w}}{\partial \alpha_{r,w}^2}\right|_{\alpha_{r,w}=0} \alpha_{r,w}^2 \\ &+ \frac{1}{3!} \left.\frac{\partial^3 C_{y,w}}{\partial \alpha_{r,w}^3}\right|_{\alpha_{r,w}=0} \alpha_{r,w}^3 + O\left(\alpha_{r,w}^4\right), \end{aligned} \tag{11}$$

where $O(\alpha_{r,w}^4)$ denotes the terms proportional to $\alpha_{r,w}^4$ and the higher powers of $\alpha_{r,w}$ which are ignored.

Combining (5) with (11), the vertical aerodynamic force on unit length of iced contact wire can be obtained according to (7).

$$F_{y,w} = a_{3,w} \dot{y}_w^3 + a_{2,w} \dot{y}_w^2 + a_{1,w} \dot{y}_w + a_{0,w}, \tag{12}$$

where the expressions of $a_{3,w}$, $a_{2,w}$, $a_{1,w}$, and $a_{0,w}$ are

$$\begin{aligned} a_{3,w} = &\frac{\rho_{\text{air}} D_w}{2U} \left[\frac{1}{6} d_3 \alpha_{0,w}^3 + \left(\frac{3}{2} l_3 + \frac{1}{6} d_2\right) \alpha_{0,w}^2 \right. \\ &\left. + \left(l_2 + \frac{1}{6} d_1 - 3 d_3\right) \alpha_{0,w} + \frac{1}{2} l_1 + \frac{1}{6} d_0 - d_2\right], \end{aligned} \tag{13}$$

$$\begin{aligned} a_{2,w} = &\frac{\rho_{\text{air}} D_w}{2} \left[-\frac{1}{2} l_3 \alpha_{0,w}^3 + \left(3 d_3 - \frac{1}{2} l_2\right) \alpha_{0,w}^2 \right. \\ &\left. + \left(3 l_3 - \frac{1}{2} l_1 + 2 d_2\right) \alpha_{0,w} + d_1 + l_2 - \frac{1}{2} l_0\right], \end{aligned} \tag{14}$$

$$\begin{aligned} a_{1,w} = &-\frac{\rho_{\text{air}} D_w U}{2} \left[d_3 \alpha_{0,w}^3 + (d_2 + 3 l_3) \alpha_{0,w}^2 \right. \\ &\left. + (d_1 + 2 l_2) \alpha_{0,w} + d_0 + l_1\right], \end{aligned} \tag{15}$$

$$a_{0,w} = \frac{\rho_{\text{air}} D_w U^2}{2} \left[l_3 \alpha_{0,w}^3 + l_2 \alpha_{0,w}^2 + l_1 \alpha_{0,w} + l_0\right]. \tag{16}$$

As for the iced messenger wire, its cross section is similar to that of iced contact wire; that is, $\lambda_m = \lambda_w$. Here the subscript m represents the messenger wire. Due to the same working environment and same order magnitude of diameters ($D_w = 14.4$ mm, $D_m \approx 9.17$ mm), the Reynolds of iced messenger wire and iced contact wire are in the same interval ($\text{Re}_w = 21110$, $\text{Re}_m = 13443$).

As a result, the drag and lift coefficients of iced contact wire and iced messenger wire are assumed to be the same. Similarly, the vertical aerodynamic force on unit length of iced messenger wire can be written as

$$F_{y,m} = a_{3,m} {\dot{y}_m}^3 + a_{2,m} {\dot{y}_m}^2 + a_{1,m} \dot{y}_m + a_{0,m}, \tag{17}$$

where the coefficient forms of $a_{3,m}$, $a_{2,m}$, $a_{1,m}$, and $a_{0,m}$ are the same as those shown in (13)–(16).

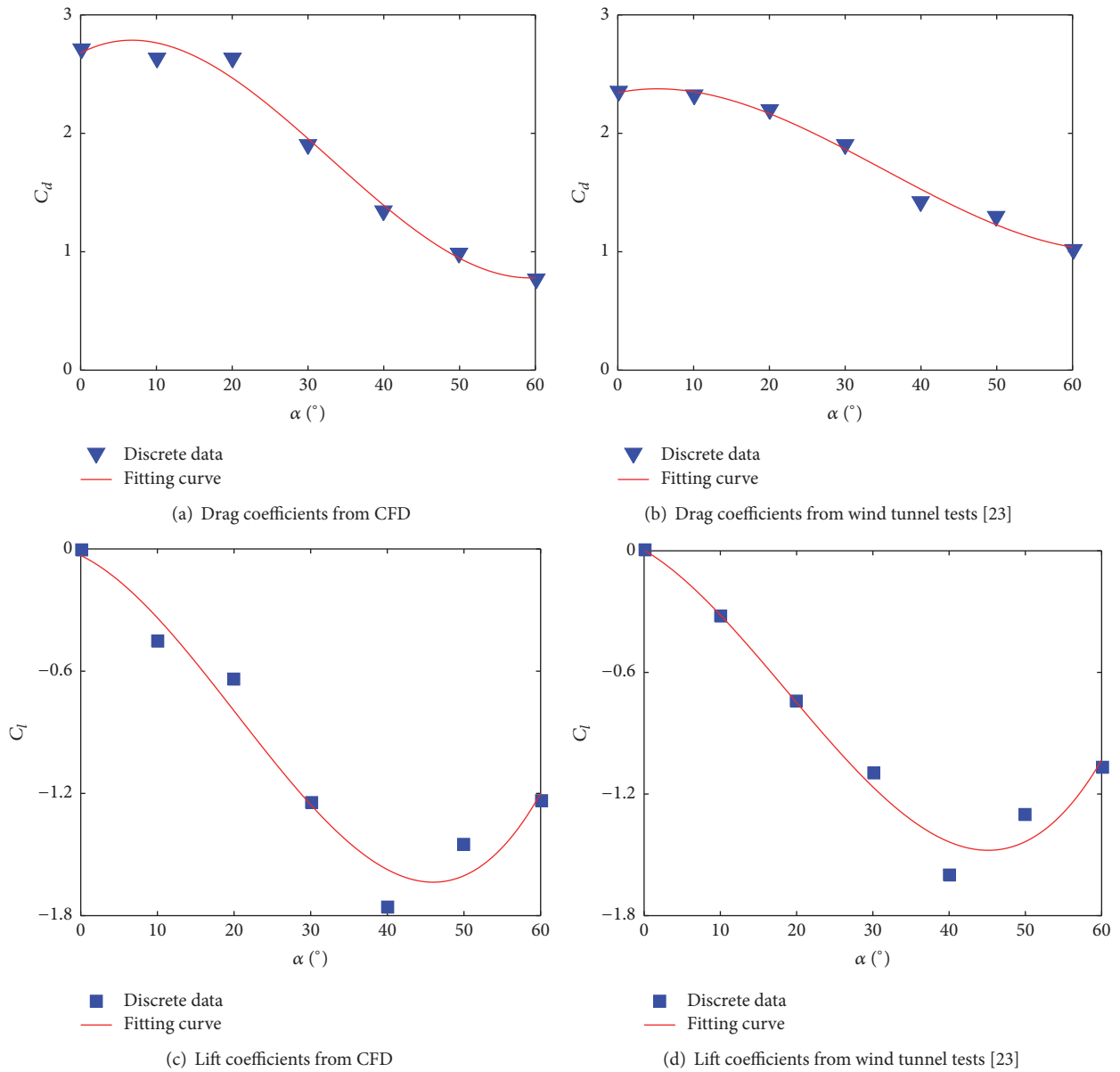

(a) Drag coefficients from CFD

(b) Drag coefficients from wind tunnel tests [23]

(c) Lift coefficients from CFD

(d) Lift coefficients from wind tunnel tests [23]

Figure 6: Comparison of drag and lift coefficients from CFD and wind tunnel tests of a D-shape section.

Table 1: Polynomial coefficients of fitting curves.

Coefficient	Value	Coefficient	Value
d_0	0.4238	l_0	0
d_1	0	l_1	1.9841
d_2	2.0079	l_2	0
d_3	0	l_3	−2.0687

4. Galloping Vibration of Catenary System

In this section, the equations of vertical motion of the simple catenary system under cross winds are derived. As shown in Figure 10, the contact wire and messenger wire can be described by the simply supported Euler-Bernoulli beams. According to the mechanical characteristics, the droppers are simplified as the nonlinear springs, in which the tensile stiffness is far larger than the compression stiffness.

The infinitesimal method is used to derive the equations of motion of the messenger and contact wires which are simplified as Euler-Bernoulli beams [28]. Figure 11 is the force

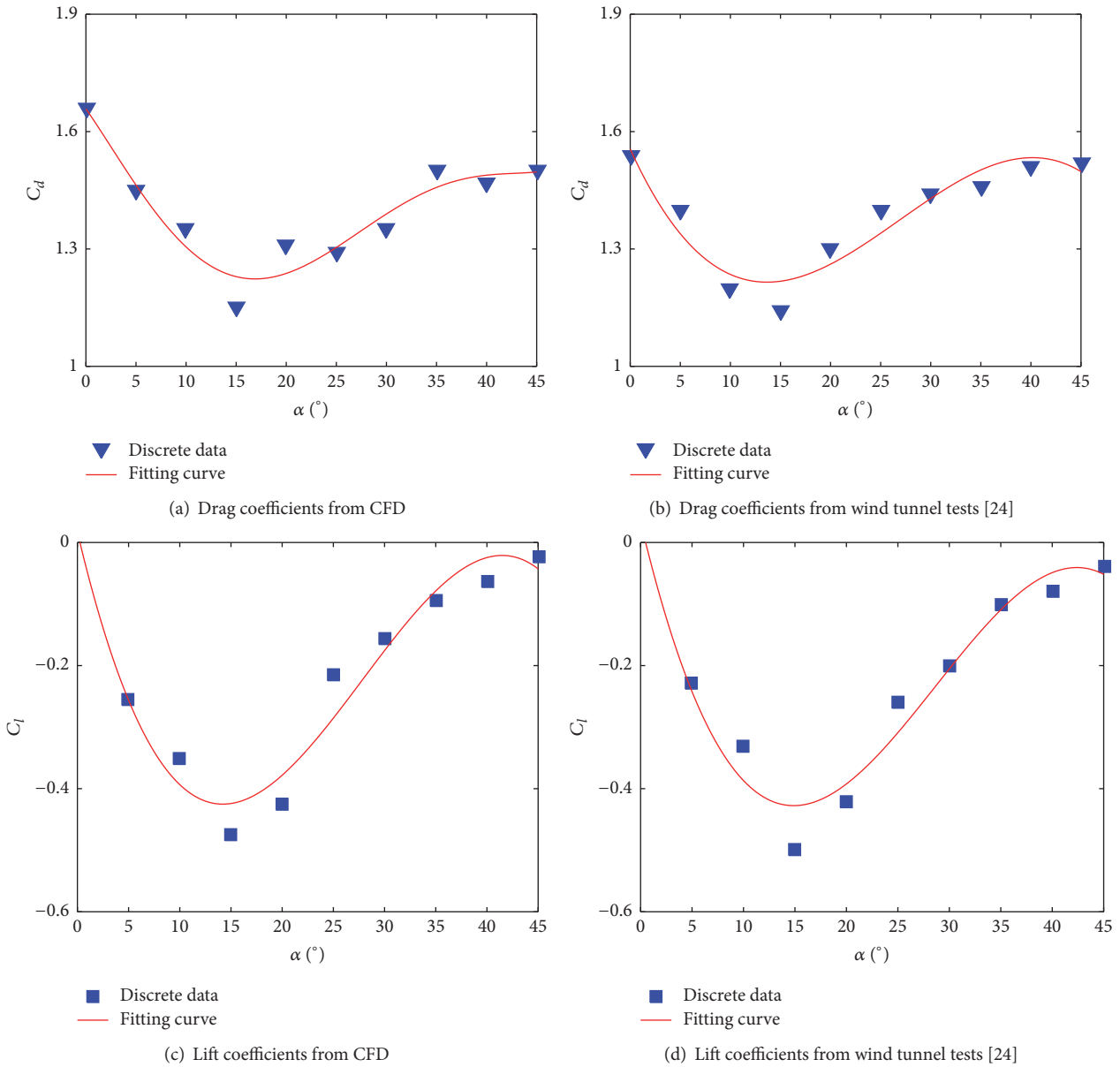

Figure 7: Comparison of drag and lift coefficients from CFD and wind tunnel tests of a square section.

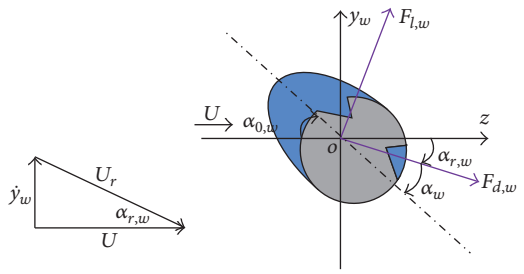

Figure 8: Galloping model of iced contact wire in the vertical direction.

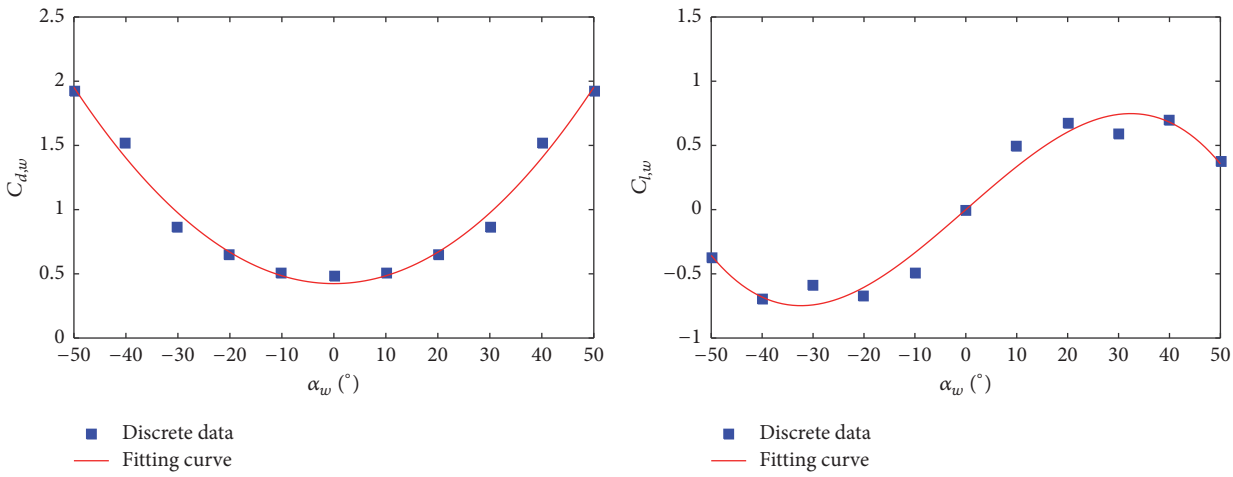

(a) Drag coefficient (b) Lift coefficient

FIGURE 9: Fitting curves.

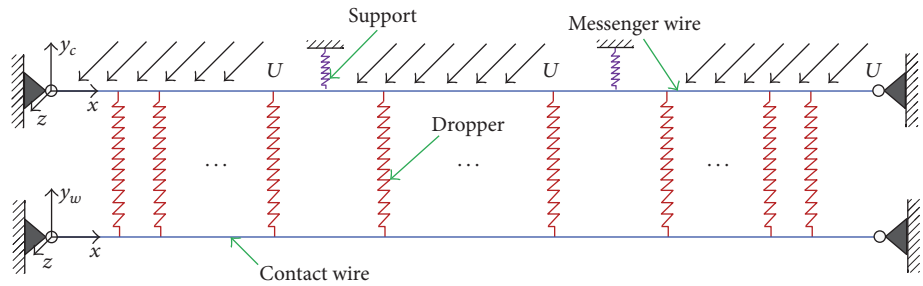

FIGURE 10: Schematic diagram of simple catenary system under cross winds.

diagram of the Euler-Bernoulli beam infinitesimal element in which $f(x,t)$ denotes the vertical force per unit length, $y(x,t)$ the vertical displacement, $\rho A(x)$ the mass per unit length, EI the bending stiffness, T the tensile force, M the bending moment, Q the shear force, and dx the length of the beam element.

Derived from Figure 11(b), the force equation of motion in the vertical direction can be expressed as

$$Q - \left(Q + \frac{\partial Q}{\partial x}dx\right) - T\sin\theta + T\sin\left(\theta + \frac{\partial\theta}{\partial x}dx\right) + f(x,t)\,dx = -\rho A(x)\,dx\frac{\partial^2 y(x,t)}{\partial t^2}. \tag{18}$$

Due to the reason that θ is relatively small, there exists the assumption $\sin\theta \approx \theta$. Therefore, (18) can be derived as

$$-\frac{\partial Q}{\partial x}dx + T\frac{\partial\theta}{\partial x}dx + f(x,t)\,dx = -\rho A(x)\,dx\frac{\partial^2 y(x,t)}{\partial t^2}. \tag{19}$$

According to the mechanical characteristic and deformation relationship introduced in material mechanics, we can obtain that

$$\theta = \frac{\partial y(x,t)}{\partial x},$$
$$Q = \frac{\partial M}{\partial x}, \tag{20}$$
$$M = -EI\frac{\partial^2 y(x,t)}{\partial x^2}.$$

Substituting (20) into (19), the equation of motion of an equal section Euler-Bernoulli beam can be written as

$$\rho A\ddot{y} + EIy'''' + Ty'' = -f(x,t). \tag{21}$$

In which $\ddot{y} = \partial^2 y/\partial t^2$, $y'''' = \partial^4 y/\partial x^4$, $y'' = \partial^2 y/\partial x^2$.

For the iced messenger wire, the lumped external forces include the elastic forces acted by droppers and the elastic force acted by masts, and the distributed external forces include the damping force and the aerodynamic force. For the iced contact wire, the lumped external forces include the elastic forces acted by droppers and the distributed external forces include the damping forces and the aerodynamic forces.

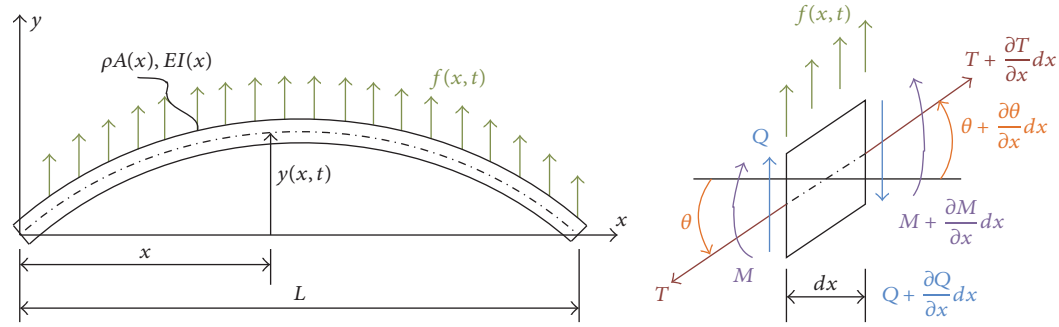

(a) Bending configuration of an Euler-Bernoulli beam [28]

(b) Free-body diagram for a beam element

FIGURE 11: Diagram of the Euler-Bernoulli beam.

Thus, the vertical vibration equation of iced messenger wire under cross winds can be derived as

$$\rho_m A_m \ddot{y}_m + C_m \dot{y}_m + EI_m y_m'''' + T_m y_m'' = -\sum_{i=1}^{b} F_{m,i} - \sum_{i=1}^{p} F_{s,i} + F_{y,m}, \tag{22}$$

in which y_m, ρ_m, A_m, C_m are the vertical displacement, linear density, area of cross section, and the structural damping coefficient, respectively. EI_m, T_m, $F_{m,i}$, b, and p denote bending stiffness, the tensile force acted on the iced messenger wire, the sum of elastic force given by ith dropper and gravity of droppers and clamps, the number of droppers, and the number of support springs.

The elastic support force acted on the messenger wire (see Figure 10) can be expressed as

$$F_{s,i} = k_s y_{m,s,i} \times \delta\left(x - x_{s,i}\right), \tag{23}$$

where k_s, $y_{m,s,i}$, $x_{s,i}$ denote the support stiffness, the vertical displacement of the messenger wire at ith support, and the location of ith support on the x axis, and δ is the Dirac function.

By repeating the above steps, the vertical vibration equation of iced contact wire under cross winds can be expressed as

$$\rho_w A_w \ddot{y}_w + C_w \dot{y}_w + EI_w y_w'''' + T_w y_w'' = -\sum_{i=1}^{b} F_{w,i} + F_{y,w}. \tag{24}$$

The coupling relations between contact wire and messenger wire are achieved by the droppers. For each dropper shown in Figure 10, the elastic forces acted on the contact wire and messenger wire, respectively, obey

$$F_{m,i} = \delta\left(x - x_i\right)\left(\frac{1}{2} m_i g + f_{d,i}\right),$$
$$F_{w,i} = \delta\left(x - x_i\right)\left(\frac{1}{2} m_i g - f_{d,i}\right), \tag{25}$$

where x_i is the location of ith dropper on the x axis; m_i is the total mass of ith dropper and clamps.

According to the mechanical characteristic, the elastic force of ith dropper can be written as

$$f_{d,i} = k_{d,i}\left(y_{m,i} - y_{w,i} + \Delta l_0\right),$$
$$k_{d,i} = \begin{cases} k_{td}, & \left(y_{m,i} - y_{w,i} + \Delta l_0\right) \geq 0 \\ k_{pd}, & \left(y_{m,i} - y_{w,i} + \Delta l_0\right) < 0, \end{cases} \tag{26}$$

where k_{td} and k_{pd} denote the tensile stiffness and compression stiffness, respectively, Δl_0 is the initial elongation of dropper, and $y_{m,i}$ and $y_{w,i}$ denote the vertical displacements of messenger wire and contact wire at the position of ith dropper.

In order to obtain the dynamic characteristic of the catenary system, the Galerkin method is adapted to discretize the partial differential equations. The main vibration mode functions are assumed as $\varphi_m(x)$ and $\varphi_w(x)$, which satisfy the boundary conditions of contact wire and messenger wire. Therefore, the solutions to vibration equations of catenary system can be expressed as

$$y_m = \sum_{i=1}^{n} \varphi_{m,i}(x)\, q_{m,i}(t) \tag{27}$$

$$y_w = \sum_{i=1}^{n} \varphi_{w,i}(x)\, q_{w,i}(t), \tag{28}$$

where $q_{m,i}(t)$ and $q_{w,i}(t)$ are the mode coordinates of messenger wire and contact wire; n is the modal truncation order.

According to [25], the main parameters of catenary system are shown in Table 2. In addition, the span of catenary is set to 10, the tensile stiffness of dropper is $k_{td} = 10^6$ N/m, the compression stiffness of dropper is $k_{pd} = 0.5 \times 10^4$ N/m, and support stiffness is $k_s = 2.5 \times 10^7$ N/m. Referring to the structure design of actual catenary, the vector position of dropper in each span obeys [3.375 10.125 16.875 23.625 30.375 37.125 43.875 50.625] (m).

Since the catenary structure is extremely complicated, the analytical expression of main vibration mode functions can hardly be derived. Thus the finite element method is applied to analyze the catenary mode for obtaining the discretized main vibration mode, as shown in Figure 12. The frequencies

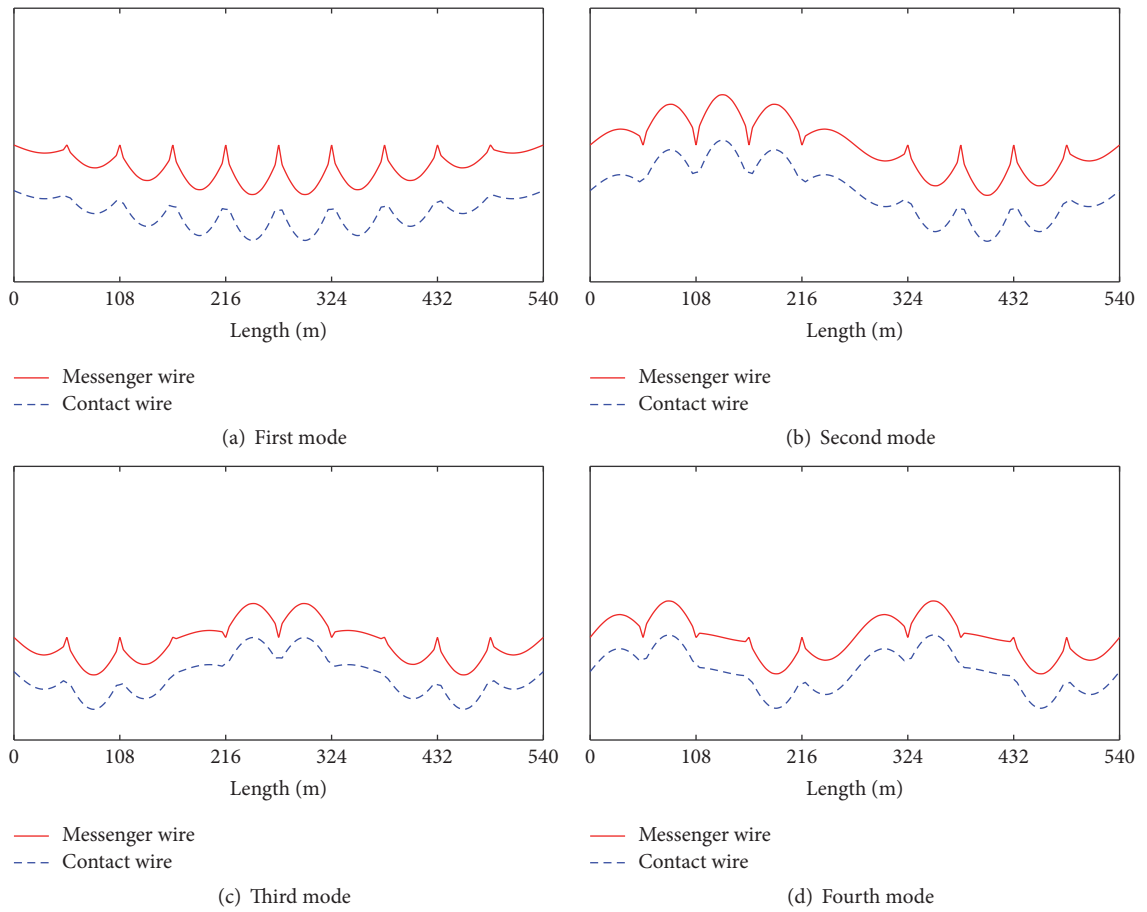

Figure 12: Vibration mode shapes of the ten-span catenary.

Table 2: Parameters of catenary model.

	Tensile force T (N)	Linear density ρA (kg/m)	Cross section area A (mm^2)	Span length l (m)
Messenger wire	14000	0.64	105.65	54
Contact wire	20000	1.43	260.58	54

are listed in Table 3. One can observe that, in the figures of first fourth modes, mode type in each span is the same. Indeed, mode type in each span is the same of every ten modes. Correspondingly, frequencies of the ten-span catenary are distributed by groups of ten.

On this basis, (27) and (28) are substituted into (22) and (24), respectively. And then multiply both sides of the equations by $\varphi_{m,j}(x)$ and $\varphi_{w,j}(x)$. Thus the ordinary differential equations of catenary system can be obtained by numerical integration. The detailed derivation is shown in the appendix.

Therefore, the discrete vibration equations of the catenary system can be rewritten in the matrix form as follows:

$$\mathbf{M}\ddot{\mathbf{q}} + \left(\mathbf{C}_l + \mathbf{C}_n\right)\dot{\mathbf{q}} + \mathbf{K}\mathbf{q} = \mathbf{Q}, \tag{29}$$

where $\mathbf{M}$ is the mass matrix, $\mathbf{C}_l$ is the linear damping matrix generated by structural damping, $\mathbf{C}_n$ is the nonlinear damping matrix generated by aerodynamic force, $\mathbf{K}$ is the stiffness matrix, $\mathbf{Q}$ is the discrete force vector, and $\mathbf{q}$ is the modal coordinates vector.

5. General Results and Discussion

5.1. Stability Analysis of Catenary System. As illustrated in [27], the aerodynamical stability of the dynamic system is mainly determined by the sign of the net damping coefficient. For the case that the net damping coefficient is greater than zero, the catenary system is aerodynamically stable. Otherwise, the catenary system is aerodynamically unstable.

It can be seen from (22) and (24) that the unstable conditions of iced messenger wire and iced contact wire, respectively, obey

$$C_w - a_{1,w} < 0, \tag{30}$$

$$C_m - a_{1,m} < 0. \tag{31}$$

Table 3: Frequencies of catenary.

Number	Frequency (Hz)
(1)	1.0495
(2)	1.0605
(3)	1.0780
(4)	1.1006
(5)	1.1267
(6)	1.1541
(7)	1.1800
(8)	1.2017
(9)	1.2161
(10)	1.2213
(11)	2.0981
(12)	2.1208
(13)	2.1562
(14)	2.2011
(15)	2.2520
(16)	2.3051
(17)	2.3561
(18)	2.3998
(19)	2.4301
(20)	2.4410

Due to the reason that the structural damping coefficients are positive, the necessary condition for the occurrence of galloping motion of iced contact wire can be derived from (15) and (30).

$$-\frac{\rho_{\text{air}} D_w U}{2}\left[d_3\alpha_{0,w}^3 + \left(d_2 + 3l_3\right)\alpha_{0,w}^2 + \left(d_1 + 2l_2\right)\alpha_{0,w} + d_0 + l_1\right] > 0. \tag{32}$$

In the above equation, the air density ρ_{air}, diameter of cross section D_w, and wind velocity U are positive. Therefore, (32) can be further reduced; namely,

$$-\left[d_3\alpha_{0,w}^3 + \left(d_2 + 3l_3\right)\alpha_{0,w}^2 + \left(d_1 + 2l_2\right)\alpha_{0,w} + d_0 + l_1\right] > 0. \tag{33}$$

Obviously, the necessary condition for the occurrence of galloping motion of iced contact wire is only affected by the drag and lift coefficients and initial icing angle. According to the parameters in Table 1, the necessary condition of instability of iced contact wire satisfies

$$\left|\alpha_{0,w}\right| > 43.4^\circ. \tag{34}$$

The above inequality is also the sufficient condition for the occurrence of galloping of iced contact wire when the structural damping is ignored.

On the assumption that the drag and lift coefficients of messenger wire and contact wire are the same in Section 3, (34) is also the necessary condition of instability of iced messenger wire.

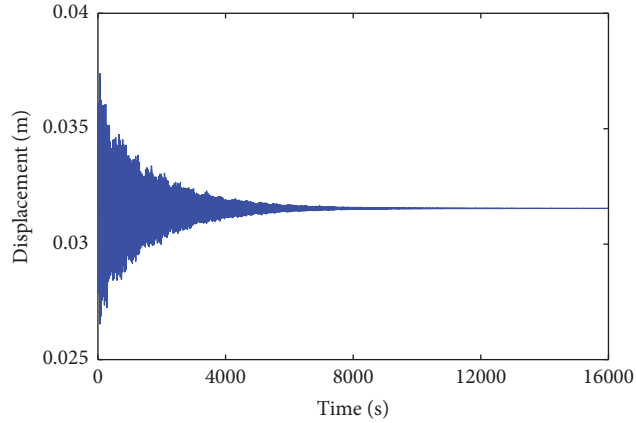

Figure 13: Vertical vibration response of the mid-point of 5th span contact wire in the condition of $\alpha_{0,m} = 43.3^\circ$ and $\alpha_{0,w} = 43.3^\circ$.

5.2. Effect of Initial Icing Angle. Considering that the main range of galloping frequency is [0.1 (Hz), 3 (Hz)] [13], the modal truncation order of the ten-span catenary is set to 20 in this paper. The Runge-Kutta method is used to calculate the dynamic response of iced catenary system numerically. In order to achieve the relatively accurate results, the integration time step is specified as 0.0008 s and the steady-state response of the mid-point of 5th span of iced contact wire is analyzed.

Keeping the parameters shown in Table 2, the effect of initial icing angle on the dynamic characteristic is conducted in this section, where the structural damping is not taken into consideration.

In the condition of $U = 15$ m/s, when the initial icing angles are $\alpha_{0,m} = 43.3^\circ$ and $\alpha_{0,w} = 43.3^\circ$, the vertical vibration response of the iced contact wire is shown in Figure 13. It is evident that the vertical vibration displacement gradually reduces to the static vertical deformation, which is mainly caused by the cross winds. Therefore, this phenomenon shown in Figure 13 is called stable vibration.

When the initial icing angles are changed to $\alpha_{0,m} = 43.4^\circ$ and $\alpha_{0,w} = 43.4^\circ$, the vertical vibration displacement of the iced contact wire is shown in Figure 14. By comparing Figure 14 with Figure 13, it can be seen that with the increase of initial icing angle, the vertical response progresses to a kind of unstable vibration with low frequency and large amplitude rather than static deformation. This is the moment when the galloping vibration of iced contact wire occurs.

In the following, the effect of single initial icing angle (initial icing angle of contact wire or initial icing angle of messenger wire) on the dynamic characteristic of the system is discussed. For the case of $\alpha_{0,m} = 40^\circ$ and $\alpha_{0,w} = 45^\circ$, only the initial icing angle of contact wire meets the condition of instability. Correspondingly, the vibration response of iced contact wire is shown in Figure 15, in which the system maintains a small amplitude vibration after reaching the steady state. For the case of $\alpha_{0,m} = 45^\circ$ and $\alpha_{0,w} = 40^\circ$, the similar dynamic phenomenon is shown in Figure 16. The main reason of the above phenomena is that the relative oscillations between contact wire and messenger wire are restricted by the droppers.

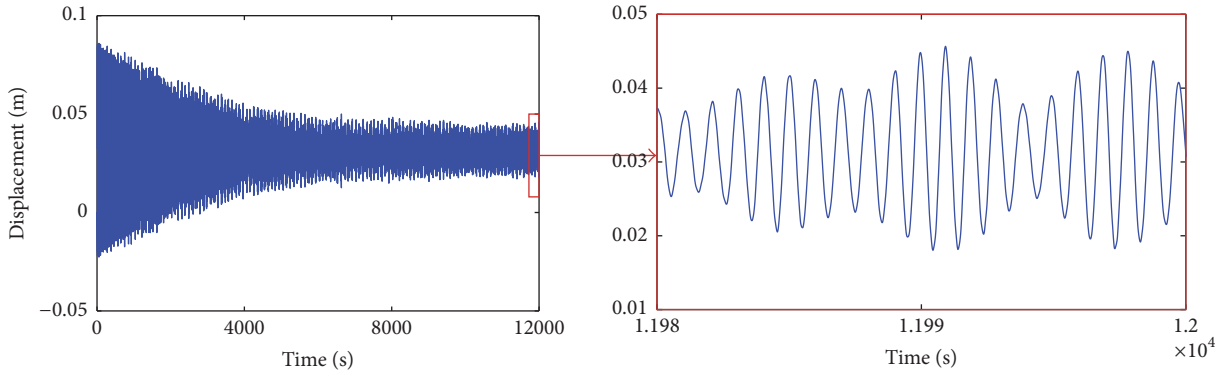

FIGURE 14: Vertical vibration response of the mid-point of 5th span contact wire in the condition of $\alpha_{0,m} = 43.4^\circ$ and $\alpha_{0,w} = 43.4^\circ$.

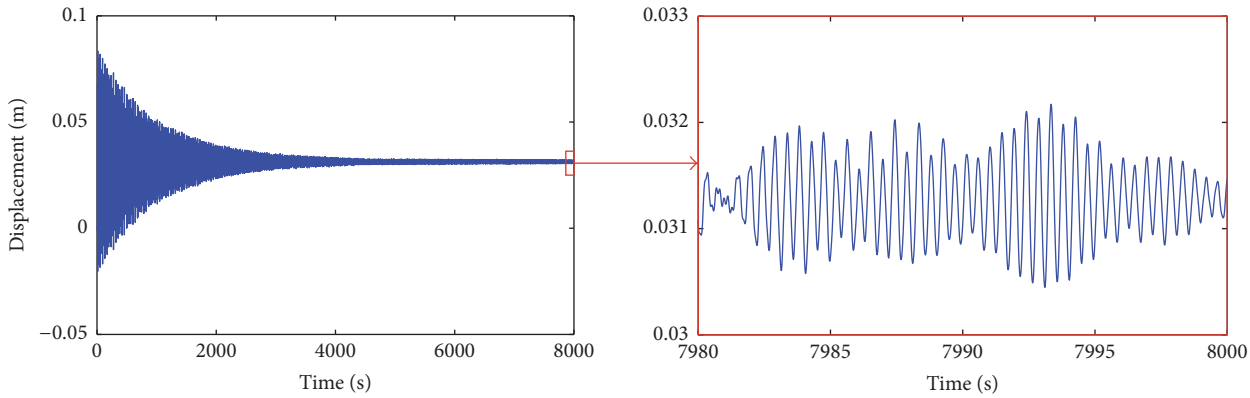

FIGURE 15: Vertical vibration response of the mid-point of 5th span contact wire in the condition of $\alpha_{0,m} = 40^\circ$ and $\alpha_{0,w} = 45^\circ$.

In addition, beating phenomenon in Figures 14–16 can be observed. The similarity of frequencies of every ten modes can cause the modal coupling while the catenary is vibrating under the action of cross winds which directly leads to the beating phenomenon. And since the neglecting of structure damping in this case, the phenomenon is particularly obvious.

When the initial icing angle of contact wire is equal to that of messenger wire, the relation between maximum vertical displacement and initial icing angle is depicted in Figure 17. It is clear that the critical initial icing angle for the occurrence of galloping motion is 43.4°, which exactly meets the condition of instability of iced contact wire obtained in Section 5.1. At the interval of 40°–43.4°, the vibration of iced catenary system is stable. Meanwhile, the wind deviation is small and changes little with the increase of initial icing angle. At the interval of 43.4°–49°, the galloping vibration of iced catenary system occurs and the max displacement becomes larger with the increase of initial icing angle.

5.3. Effect of Structural Damping. As shown in expression (34), the stability condition is closely related to the structural damping. For most of actual engineering structures, the structure damping is usually characterized by the proportional damping in numerical calculations. Thus, the proportional damping matrix can be expressed as

$$\mathbf{C}_l = \alpha\mathbf{M} + \beta\mathbf{K}, \tag{35}$$

where damping coefficients can be derived as [29]

$$\begin{Bmatrix} \zeta_1 \\ \zeta_2 \\ \vdots \\ \zeta_n \end{Bmatrix} = \frac{1}{2} \begin{bmatrix} \frac{1}{\omega_1} & \omega_1 \\ \frac{1}{\omega_2} & \omega_2 \\ \vdots & \vdots \\ \frac{1}{\omega_n} & \omega_n \end{bmatrix} \begin{Bmatrix} \alpha \\ \beta \end{Bmatrix}, \tag{36}$$

in which ω_n is the circular frequency, ζ_n is the damping ratio, and n is the number of modes which is set to 20. The estimation of the Rayleigh coefficients can be performed by solving the overdetermined equation (36) by least-squares solution. According to [30], the damping ratio is set to 0.0013, and the coefficients are $\alpha = 0.0125$, $\beta = 0.0001$.

After considering the structure damping, the vertical vibration responses of contact wire with different initial icing

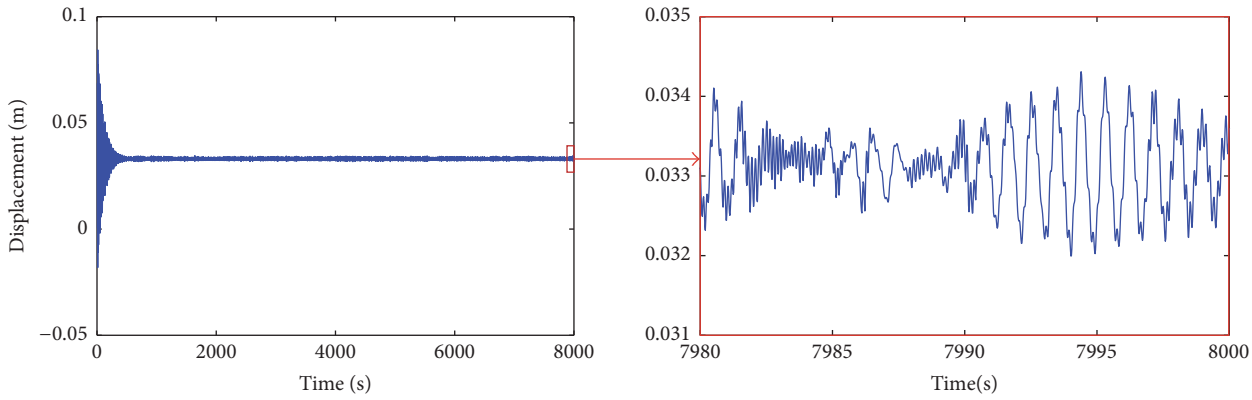

FIGURE 16: Vertical vibration response of the mid-point of 5th span contact wire in the condition of $\alpha_{0,m} = 45^\circ$ and $\alpha_{0,w} = 40^\circ$.

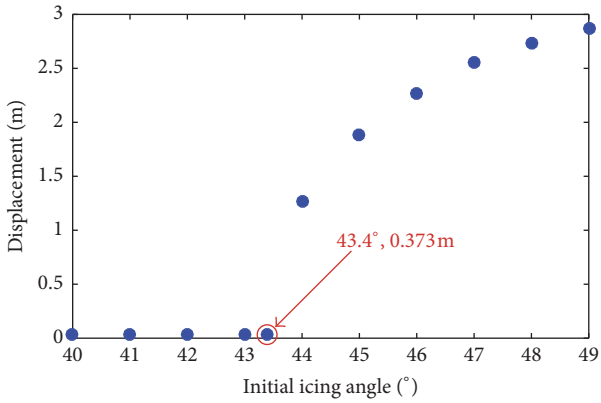

FIGURE 17: Relation between maximum displacement and initial icing angle.

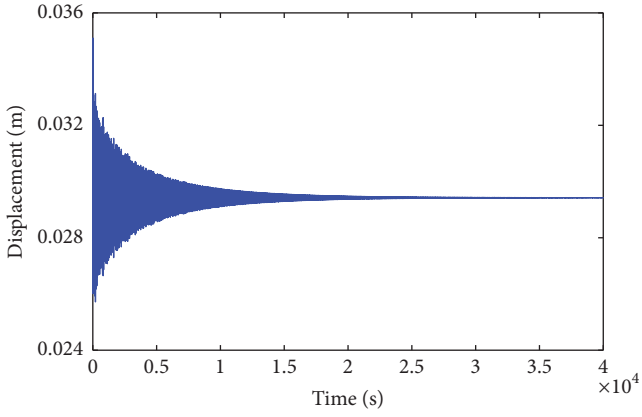

FIGURE 18: Vertical vibration response of the mid-point of 5th span contact wire in the condition of $\alpha_{0,m} = 44.7^\circ$ and $\alpha_{0,w} = 44.7^\circ$.

angles are analyzed. As shown in Figure 18, the contact wire is still stable in the conditions of $\alpha_{0,m} = 44.7^\circ$ and $\alpha_{0,w} = 44.7^\circ$. This phenomenon suggests that the structural damping can raise the critical initial icing for unstable station.

When the initial icing angles are $\alpha_{0,m} = 44.8^\circ$ and $\alpha_{0,w} = 44.8^\circ$, the system becomes unstable and the galloping oscillation appears, as shown in Figure 19. Therefore, the new critical initial icing angle with the effect of structural damping is about $\alpha_{0,m} = 44.8^\circ$ and $\alpha_{0,w} = 44.8^\circ$. Overall, the structural damping has a positive contribution to the motion stability of iced catenary system.

5.4. Effect of Wind Velocity. Taking the structural damping into consideration, the effect of wind velocity on the vibration response of iced catenary system is further discussed in this section. In the range of wind velocity 1 m/s–35 m/s, the Reynolds numbers of both iced contact wire and messenger wire are in the transcritical scope. When the wind velocity is in the range, the drag and lift coefficients are available.

For the case of $\alpha_{0,m} = 45^\circ$ and $\alpha_{0,w} = 45^\circ$, the vertical vibration response of iced contact wire is calculated in the condition of $U = 12.4$ m/s, as shown in Figure 20. It is clear that the system response converges to a static deformation, which is the deviation caused by the cross winds. This phenomenon suggests that the iced catenary system is stable at this moment. Keeping the initial icing angles of contact wire and messenger wire constant, the wind velocity is changed to $U = 12.5$ m/s. Correspondingly, a periodic vibration with low frequency appears in Figure 21, which indicates the instability phenomenon.

The relation between maximum vibration in the steady-state and wind velocity is further analyzed, as shown in Figure 22. When the initial icing angle is 45°, the critical wind velocity of stability is $U = 12.5$ m/s. When the wind velocity is smaller than the critical value, the iced catenary system is stable. While the wind velocity is larger than the critical value, the galloping vibration occurs and the vibration displacement turns to be larger with the increase of wind velocity.

6. Conclusion

In this paper, the galloping vibration of iced catenary system under cross winds has been investigated. By FLUENT simulation, the lift and drag coefficients of quasi-steady aerodynamic force acted on the iced catenary system have been calculated. By fitting the discrete simulation data, the expression of the vertical aerodynamic force has been further

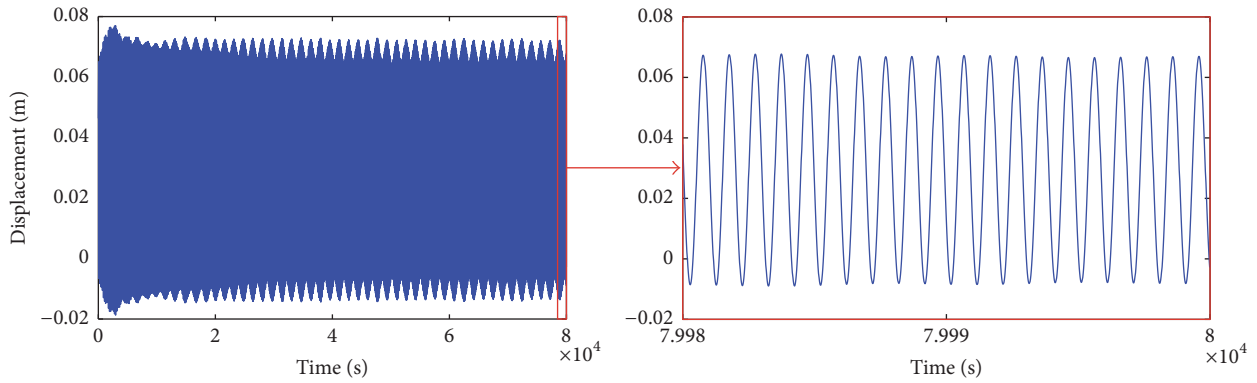

Figure 19: Vertical vibration response of the mid-point of 5th span contact wire in the condition of $\alpha_{0,m} = 44.8^\circ$ and $\alpha_{0,w} = 44.8^\circ$.

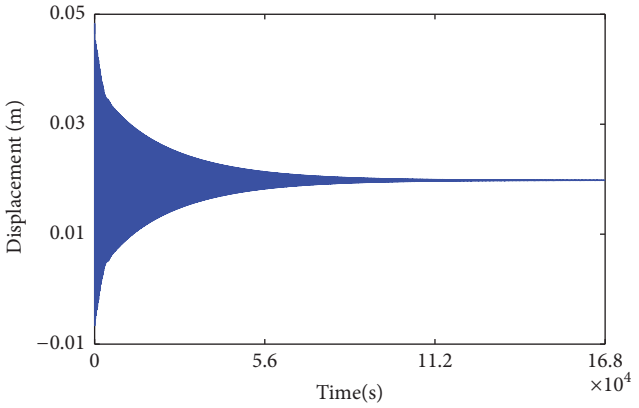

Figure 20: Vertical vibration response of the mid-point of 5th span contact wire in the condition of $U = 12.4$ m/s.

derived. Then the necessary condition of system stability has been further obtained based on the Den Hartog galloping mechanism. Moreover, the vibration equations of iced catenary system have been solved by the Runge-Kutta method and the corresponding responses have been analyzed by the waveform. Meanwhile, the analysis of varying parameters, for instance, the initial icing angle, structural damping, and wind velocity, has been conducted. According to the analysis results, the following conclusions can be obtained.

(1) As for vertical galloping vibration of iced catenary system, the critical condition of motion stability is mainly determined by initial icing angle, wind velocity, and structural damping.

(2) For the case of stable vibration, the dynamic response of iced catenary system usually reduces to a static wind deviation. For the case of unstable vibration, the galloping motion occurs in the iced catenary system.

(3) Suspended on the messenger wire, the stability of iced contact wire is improved when the initial icing angles of messenger and contact wires are different.

(4) Increasing the structural damping can reduce the chance that the galloping motion occurs. In the actual engineering case, mechanical damping can be used to restrain the galloping oscillation of the catenary.

Appendix

$$
\begin{aligned}
&\rho_m A_m \sum_{i=1}^{n} \left(\int_0^{l_c} \varphi_{m,j} \varphi_{m,i} dx \right) \ddot{q}_{m,i} \\
&+ C_m \sum_{i=1}^{n} \left(\int_0^{l_c} \varphi_{m,j} \varphi_{m,i} dx \right) \dot{q}_{m,i} \\
&+ \left[EI_m \sum_{i=1}^{n} \left(\int_0^{l_c} \varphi_{m,j} \varphi_{m,i}^{\prime\prime\prime\prime} dx \right) \right. \\
&\left. + T_m \sum_{i=1}^{n} \left(\int_0^{l_c} \varphi_{m,j} \varphi_{m,i}^{\prime\prime} dx \right) \right] q_{m,i} \\
&= -\sum_{k=1}^{b} \sum_{i=1}^{n} k_{d,k} \varphi_{m,j} \left(x_{d,k} \right) \varphi_{m,i} \left(x_{d,k} \right) q_{m,i} \\
&+ \sum_{k=1}^{b} \sum_{i=1}^{n} k_{d,k} \varphi_{m,j} \left(x_{d,k} \right) \varphi_{w,i} \left(x_{d,k} \right) q_{w,i} \\
&- \sum_{k=1}^{b} k_{d,k} \Delta l_{0,k} \varphi_{m,j} \left(x_{d,k} \right) - \frac{1}{2} g \sum_{k=1}^{b} m_{d,k} \varphi_{m,j} \left(x_{d,k} \right) \\
&- \sum_{k=1}^{p} \sum_{i=1}^{n} k_{s,k} \varphi_{m,j} \left(x_{s,k} \right) \varphi_{m,i} \left(x_{s,k} \right) q_{m,i} \\
&+ a_{m,3} \sum_{i=1}^{n} \sum_{l=1}^{n} \sum_{h=1}^{n} \left(\int_0^{l_c} \varphi_{m,j} \varphi_{m,i} \varphi_{m,l} \varphi_{m,h} dx \right) \\
&\cdot \dot{q}_{m,i} \dot{q}_{m,l} \dot{q}_{m,h} + a_{m,2} \sum_{i=1}^{n} \sum_{l=1}^{n} \left(\int_0^{l_c} \varphi_{m,j} \varphi_{m,i} \varphi_{m,l} dx \right) \\
&\cdot \dot{q}_{m,i} \dot{q}_{m,l} + a_{m,1} \sum_{i=1}^{n} \left(\int_0^{l_m} \varphi_{m,j} \varphi_{m,i} dx \right) \dot{q}_{m,i} \\
&+ a_{m,0} \int_0^{l_m} \varphi_{m,j} dx = 0, \quad j = 1, 2, \ldots, n, \\
&\rho_w A_w \sum_{i=1}^{n} \left(\int_0^{l_w} \varphi_{w,j} \varphi_{w,i} dx \right) \ddot{q}_{w,i}
\end{aligned}
\tag{A.1}
$$

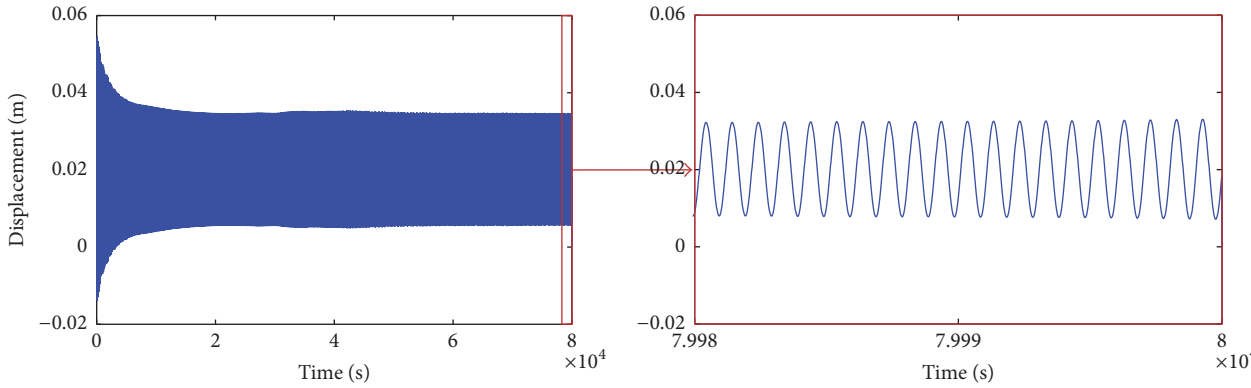

FIGURE 21: Vertical vibration response of the mid-point of 5th span contact wire in the condition of $U = 12.5$ m/s.

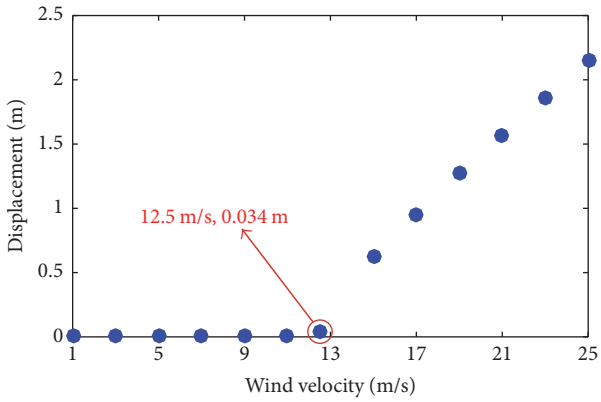

FIGURE 22: Relation between maximum vibration displacement and wind velocity.

$$
\begin{aligned}
&+ C_w \sum_{i=1}^{n} \left(\int_0^{l_w} \varphi_{w,j} \varphi_{w,i} dx \right) \dot{q}_{w,i} \\
&+ \left[EI_w \sum_{i=1}^{n} \left(\int_0^{l_c} \varphi_{w,j} \varphi_{w,i}'''' dx \right) \right. \\
&\left. + T_w \sum_{i=1}^{n} \left(\int_0^{l_c} \varphi_{w,j} \varphi_{w,i}'' dx \right) \right] q_{w,i} \\
&= - \sum_{k=1}^{b} \sum_{i=1}^{n} k_{d,k} \varphi_{w,j} \left(x_{d,k} \right) \varphi_{w,i} \left(x_{d,k} \right) q_{w,i} \\
&+ \sum_{k=1}^{b} \sum_{i=1}^{n} k_{d,k} \varphi_{w,j} \left(x_{d,k} \right) \varphi_{c,i} \left(x_{d,k} \right) q_{c,i} \\
&+ \sum_{k=1}^{b} k_{d,k} l_{0d,k} \varphi_{w,j} \left(x_{d,k} \right) - \frac{1}{2} g \sum_{k=1}^{b} m_{d,k} \varphi_{w,j} \left(x_{d,k} \right) \\
&+ a_{w,3} \sum_{i=1}^{n} \sum_{l=1}^{n} \sum_{h=1}^{n} \left(\int_0^{l_w} \varphi_{w,j} \varphi_{w,i} \varphi_{w,l} \varphi_{w,h} dx \right) \dot{q}_{w,i} \dot{q}_{w,l} \dot{q}_{w,h} \\
&+ a_{w,2} \sum_{i=1}^{n} \sum_{l=1}^{n} \left(\int_0^{l_w} \varphi_{w,j} \varphi_{w,i} \varphi_{w,l} dx \right) \dot{q}_{w,i} \dot{q}_{w,l} \\
&+ a_{w,1} \sum_{i=1}^{n} \left(\int_0^{l_w} \varphi_{w,j} \varphi_{w,i} dx \right) \dot{q}_{w,i} + a_{w,0} \int_0^{l_w} \varphi_{w,j} dx \\
&= 0, \quad j = 1, 2, \ldots, n.
\end{aligned}
\tag{A.2}
$$

Conflicts of Interest

The authors declare that there are no conflicts of interest regarding the publication of this paper.

Acknowledgments

This work was supported by the National Nature Science Foundation of China (Grants nos. 11372258 and 11702228) and the Fundamental Research Funds for the Central Universities (2682017CX087).

References

[1] M. T. Stickland and T. J. Scanlon, "An investigation into the aerodynamic characteristics of catenary contact wires in a cross-wind," *Proceedings of the Institution of Mechanical Engineers, Part F: Journal of Rail and Rapid Transit*, vol. 215, no. 4, pp. 311–318, 2001.

[2] Y. L. Guo, G. X. Li, and C. Y. You, "Transmission Line Galloping, China Electric Power Express".

[3] J. P. Den Hartog, "Transmission line vibration due to sleet," *Transactions of the American Institute of Electrical Engineers*, vol. 51, no. 4, pp. 1074–1076, 1932.

[4] O. Nigol and P. G. Buchan, "Conductor galloping part I: den hartog mechanism," *IEEE Transactions on Power Apparatus and Systems*, vol. 100, no. 2, pp. 699–707, 1981.

[5] O. Nigol and P. G. Buchan, "Conductor galloping part II: torsional mechanism," *IEEE Transactions on Power Apparatus and Systems*, vol. 100, no. 2, pp. 708–720, 1981.

[6] P. Yu, N. Popplewell, and A. H. Shah, "Instability trends of inertially coupled galloping. Part I: Initiation," *Journal of Sound and Vibration*, vol. 183, no. 4, pp. 663–678, 1995.

[7] P. Yu, N. Popplewell, and A. H. Shah, "Instability trends of inertially coupled galloping. Part II: periodic vibrations," *Journal of Sound and Vibration*, vol. 183, no. 4, pp. 679–691, 1995.

[8] A. Luongo and G. Piccardo, "Linear instability mechanisms for coupled translational galloping," *Journal of Sound and Vibration*, vol. 288, no. 4-5, pp. 1027–1047, 2005.

[9] K. F. Jones, "Coupled vertical and horizontal galloping," *Journal of Engineering Mechanics*, vol. 118, no. 1, pp. 92–107, 1992.

[10] Y. M. Desai, A. H. Shah, and N. Popplewell, "Galloping analysis for two-degree of-freedom oscillator," *Journal of Engineering Mechanics*, vol. 116, no. 12, pp. 2583–2602, 1990.

[11] P. Yu, M. Desai, A. H. Shah, and N. Popplewell, "Three-degree-of-freedom model for galloping. Part I: formulation," *Journal of Engineering Mechanics*, vol. 119, no. 12, pp. 2404–2425, 1993.

[12] P. Yu, Y. M. Desai, N. Popplewell, and A. H. Shah, "Three-degree-of-freedom model for galloping. Part II: Solutions," *Journal of Engineering Mechanics*, vol. 119, no. 12, pp. 2426–2448, 1993.

[13] Y. M. Desai, P. Yu, N. Popplewell, and A. H. Shah, "Finite element modelling of transmission line galloping," *Computers and Structures*, vol. 57, no. 3, pp. 407–420, 1995.

[14] Y. M. Desai, P. Yu, A. H. Shah, and N. Popplewell, "Perturbation-based finite element analyses of transmission line galloping," *Journal of Sound and Vibration*, vol. 191, no. 4, pp. 469–489, 1996.

[15] Q. Zhang, N. Popplewell, and A. H. Shah, "Galloping of bundle conductor," *Journal of Sound and Vibration*, vol. 234, no. 1, pp. 115–134, 2000.

[16] R. Keutgen and J.-L. Lilien, "Benchmark cases for galloping with results obtained from wind tunnel facilities - validation of a finite element model," *IEEE Transactions on Power Delivery*, vol. 15, no. 1, pp. 367–374, 2000.

[17] Z. Yan, Z. Li, E. Savory, and W. E. Lin, "Galloping of a single iced conductor based on curved-beam theory," *Journal of Wind Engineering and Industrial Aerodynamics*, vol. 123, pp. 77–87, 2013.

[18] M. T. Stickland, T. J. Scanlon, I. A. Craighead, and J. Fernandez, "An investigation into the mechanical damping characteristics of catenary contact wires and their effect on aerodynamic galloping instability," *Proceedings of the Institution of Mechanical Engineers F: Journal of Rail and Rapid Transit*, vol. 217, no. 2, pp. 63–71, 2003.

[19] Q. Xie, W. Wang, and H. R. Ruo, "Wind tunnel test on aerodynamic force characteristics of ice coating contact wire for high speed railway," *China Railway Science*, vol. 35, no. 1, pp. 78–84, 2014.

[20] Y. Song, Z.-G. Liu, and H.-R. Wang, "Study on aerodynamic parameters and wind vibration responses of iced contact wires of high-speed railways," *Journal of the China Railway Society*, vol. 36, no. 9, pp. 20–27, 2014.

[21] Y. Song, Z. Liu, H. Wang, X. Lu, and J. Zhang, "Nonlinear analysis of wind-induced vibration of high-speed railway catenary and its influence on pantograph–catenary interaction," *Vehicle System Dynamics*, vol. 54, no. 6, pp. 723–747, 2016.

[22] E. H. Dowell, *A Modern Course in Aeroelasticity Fifth Revised and Enlarged Edition*, vol. 217, Springer, Durham, NC, USA, 5th edition, 2015.

[23] J. Chadha and W. Jaster, "Influence of turbulence on the galloping instability of iced conductors," *IEEE Transactions on Power Apparatus and Systems*, vol. 94, no. 5, pp. 1489–1499, 1975.

[24] V. Mukhopadhyay and J. Dugundji, "Wind excited vibration of a square section cantilever beam in smooth flow," *Journal of Sound and Vibration*, vol. 45, no. 3, pp. 329–339, 1976.

[25] J. Ambrósio, J. Pombo, M. Pereira, P. Antunes, and A. Mósca, "Recent developments in pantograph-catenary interaction modelling and analysis," *International Journal of Railway Technology*, vol. 1, no. 1, pp. 249–278, 2012.

[26] H. J. Cao, *The study of aerodynamic characteristics and galloping of ice-coated transmission line*, Huazhong University of Science & Technology, Wuhan, China, 2013.

[27] R. D. Blevins, *Flow-Induced Vibrations*, Van Nostrand Reinhold, NY, USA, 2nd edition, 1990.

[28] L. Meirovitch and R. Parker, "Fundamentals of vibrations," *Applied Mechanics Reviews*, 2001.

[29] P. Nåvik, A. Rønnquist, and S. Stichel, "Identification of system damping in railway catenary wire systems from full-scale measurements," *Engineering Structures*, vol. 113, pp. 71–78, 2016.

[30] S. Bruni, J. Ambrosio, A. Carnicero et al., "The results of the pantograph-catenary interaction benchmark," *Vehicle System Dynamics*, vol. 53, no. 3, pp. 412–435, 2015.

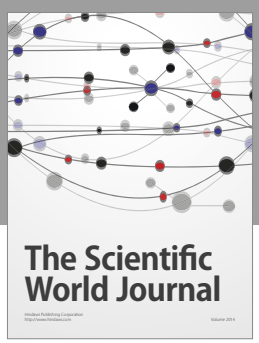

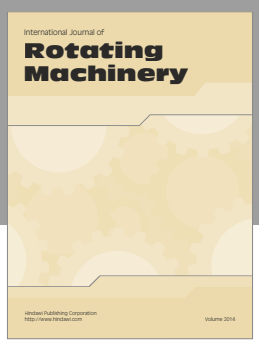

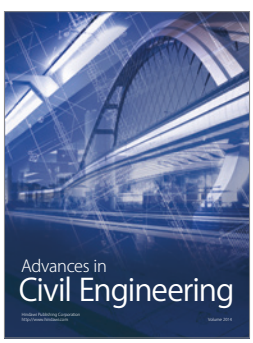

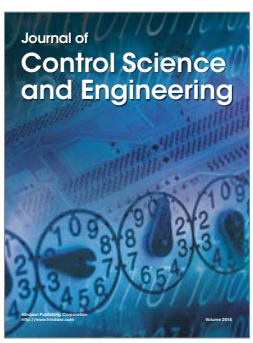

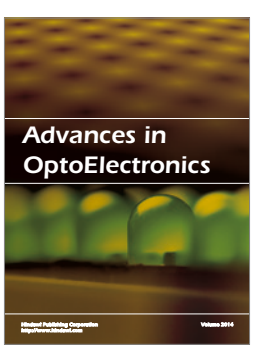

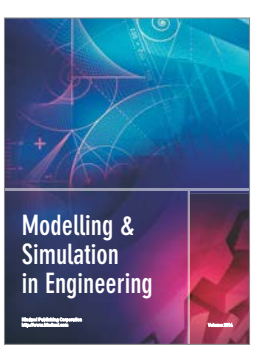

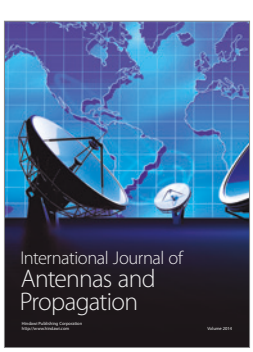

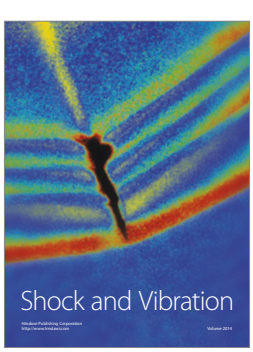

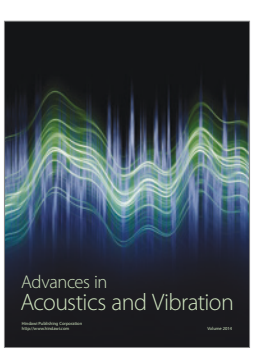

Hindawi

Submit your manuscripts at
https://www.hindawi.com